small structures
www.small-structures.com

Minimizing Intersheet Junction Resistivity via Au_4Cu_2 Nanocluster-Based Connectivity in Mo_2TiC_2 MXene for Symmetric Supercapacitor Device

Tehseen Nawaz, Muhammad Ahmad, Iftikhar Hussain, Xi Chen, B. Moses Abraham, Shengli Zhuang, Kam Hung Low, Kaili Zhang,* and Jian He**

MXenes with their intrinsic metallic conductivity and redox versatility have emerged as frontrunners in the search for advanced energy storage materials. However, their energy storage capabilities are often hindered by the limited accessibility of electrolytes to active sites and enhanced electrical resistance due to the susceptibility to layer restacking. To address these challenges, a novel, ultrasmall Au_4Cu_2 nanocluster, strategically embedded within Mo_2TiC_2 MXene layers, is introduced. This integration is facilitated through precise interfacial local interactions, which govern the regulation of interlayer electron flow. The Au_4Cu_2 nanocluster modifies the local electron density, promoting a gradient in electronic conductivity throughout the MXene layers and acting as a nanoscopic bridge that counters the tendency for restacking. This approach markedly enhances the charge transfer efficiency and, consequently, the charge storage capacity. The nanoclusters/MXene composite-based symmetric supercapacitor provides superior energy density and power density. The findings reveal a sophisticated interface engineering strategy for the prevention of interlayer restacking of MXenes that significantly elevates their ability to store charge.

1. Introduction

The field of 2D materials began with graphene and has rapidly expanded to include a vast array of materials with promising electronic and optoelectronic properties.[1–3] Networks of in-plane-aligned nanosheets are arranged in geometrical morphology suitable for thin film development. In contrast to nanotube networks, large-area conformal intersheet connections form by assembly of adjacent nanosheets, which facilitate effective charge transfer whereas nanotube networks require more complex interactions and nanoparticle arrays that often necessitate passivation to avert charge trapping attributed to the nanosheets' basal planes lacking flexible bonds. Leveraging the huge diversity through the 2D group of materials facilitates the tailoring of conducting, semiconducting, dielectric, and electrochemically active networks, which has induced the development of diverse devices, such as transistors,[4,5] photodetectors,[6,7] capacitors,[8] and supercapacitors.[9–11]

T. Nawaz, S. Zhuang, K. H. Low, J. He
Department of Chemistry
The University of Hong Kong
Hong Kong 999077, Hong Kong
E-mail: jianhe@hku.hk

T. Nawaz
Department of Chemistry
University of Oxford
Oxford OX1 3TA, UK

M. Ahmad, I. Hussain, X. Chen, K. Zhang
Department of Mechanical Engineering
City University of Hong Kong
83 Tat Chee Avenue, Kowloon, Hong Kong
E-mail: mahmadrt90@gmail.com; kaizhang@cityu.edu.hk

The ORCID identification number(s) for the author(s) of this article can be found under https://doi.org/10.1002/sstr.202400664.

M. Ahmad, B. M. Abraham
Department of Material Science and Engineering
Drexel University
Philadelphia, PA 19104, USA

M. Ahmad
School of Energy and Environment
City University of Hong Kong
83 Tat Chee Avenue, Kowloon 999077, Hong Kong

B. M. Abraham
Department of Chemical Engineering
Indian Institute of Technology Kanpur
Kanpur 208016, India

J. He
State Key Laboratory of Synthetic Chemistry
The University of Hong Kong
Hong Kong 999077, Hong Kong

DOI: 10.1002/sstr.202400664

MXenes are 2D materials constituting transition metal carbides, nitrides, and carbonitrides with characteristic surface terminations including –F, –O, –Cl, and –OH.[12,13] Their remarkable metallic conductivity, tunable interlayer spacing, redox capabilities, and versatile surface chemistry present them as potential candidates for energy storage applications.[14–16] MXenes demonstrate fast intercalation of various cations between their layers, facilitating their application as electrodes in advanced metal-ion capacitors and batteries with multiple charge carriers.[17–21] Anasori et al. discovered Mo_2TiC_2 MXene, characterized by outer layers of molybdenum sandwiching a central layer of titanium, showing promise for energy storage.[22]

However, MXenes, like other 2D materials, are prone to irreversible agglomeration caused by van der Waals forces, which can induce reduction in interlayer spacing and a subsequent decrease in specific surface area.[23] This can diminish the number of active sites and inhibit ion transportation thereby reducing the electrochemical activity and reducing its capacity for high-density energy storage.[24,25] To overcome these obstacles, MXene-based materials can be engineered to facilitate access to nanospaces and enhance ion diffusion.[26–29] Therefore, it is crucial to tailor the interlayer spacing of MXenes to augment their electrolyte-available surface area and improve the charge mobility dynamics to accomplish their full potential for charge storage.[30] The hybridization of MXenes with low-dimensional entities, like nanoparticles and/or nanotubes, can mitigate the restacking ability to some degree.[31,32] Yet, achieving a uniform dispersion of nanoscale entities remains a significant challenge due to their own tendency toward aggregation.

Ultrasmall metal nanoclusters that close the gap between individual atoms and larger nanoparticles with sizes ranging from 1 to 3 nm present a viable solution.[33–36] These nanoclusters are stabilized by a protective ligand that prevents agglomeration and enhances cluster stability.[37–39] The fact that metal nanoclusters do not aggregate makes them perfect candidates for integrating with MXenes, allowing them to disperse on the surface and prevent single-layered MXenes from restacking. To the best of our knowledge, no report shared integration of atomically precise ultrasmall metal nanocluster to prevent the restacking challenge of MXene.

For the first time, we demonstrate a unique approach for the fabrication of Au_4Cu_2 NC/Mo_2TiC_2 composite (where NC refers to nanocluster) using the chemical bath deposition method under mild conditions. The fabrication of Au_4Cu_2 NC in Mo_2TiC_2 MXene showed excellent morphological characteristics such as homogeneous dispersion of metal nanoclusters analyzed by utilizing advanced morphological techniques. The novel atomically precise Au_4Cu_2 NC was integrated within Mo_2TiC_2 MXene layers to form locally coordinated interaction and control the regulation of the interlayer electronic conduction. The local electron density of Au_4Cu_2 NC enhanced the charge transfer by forming a gradient in electronic conductivity across the MXene layers via serving as interlayer nanoscopic bridges inhibiting restacking, thereby amplifying the charge storage capacity.

2. Results and Discussions

The synthesis of doped Au_4Cu_2 NC was accomplished through a coreduction approach utilizing $HAuCl_4{\cdot}3H_2O$ and $CuSO_4{\cdot}2H_2O$ as metal precursors, $NaBH_4$ as the reducing agent, and a combination of 2,4-DMBTH and dppe as stabilizing ligands. A two-phase synthesis method was used at room temperature, with detailed procedural steps provided in the Supplementary Information. To obtain high-quality crystals for single-crystal X-ray diffraction (SCXRD), a slow diffusion technique was employed: methanol was gradually introduced into a dichloromethane (DCM) solution containing the NC at 4 °C, yielding dark crystals (Figure S1, Supporting Information). The overall atomic arrangement of the bimetallic NC is illustrated in **Figure 1**a.

SCXRD analysis revealed that the NC crystallizes in the centrosymmetric monoclinic space group C 2/c with a reliability factor (R) of 6.13%. The obtained molecular formula was further verified by electrospray ionization mass spectrometry (ESI-MS), a widely used technique for determining the mass and structural integrity of nanoclusters. The ESI-MS spectrum (Figure 1b) displays a prominent peak at m/z 2137.092, corresponding to the $[Au_4Cu_2(2,4\text{-DMBT})_6(\text{dppe}) + H]^{+1}$ ion. The close match between the experimental isotopic distribution and theoretical simulations (Figure 1b inset) conclusively confirms the NC composition. UV-Vis absorption spectra revealed that Au_4Cu_2 NC had absorption peaks at 324 nm as depicted in Figure 1c.

The bimetallic framework within the Au_4Cu_2 NC is further detailed by the tricoordination of each copper atom with 2,4-DMBT ligands, resulting in the formation of a $Cu(SR)_3$ motif, as depicted in Figure 1d. Subsequent analysis reveals that the sulfur atoms within these tricoordinate moieties facilitate additional coordination with gold atoms. Notably, two of the gold atoms serve as junctures for the tricoordinate copper moieties, creating two [−SR−Au−SR−] staple motifs (see Figure 1e). Additionally, the remaining two gold atoms manifest a divergent coordination environment, anchoring a thiolate ligand on one side and a phosphine ligand on the other, expressing as [−PR−Au−SR−] motif as shown in Figure 1f. Significantly, the dppe ligand exhibits exclusive coordination with gold atoms.

The architectural intricacies of the Au_4Cu_2 NC are depicted in **Figure 2**a,b, where a hexatomic chair conformation is observed. Within this arrangement, two $Cu(SR)_3$ motifs are designated as S_1, S_2, S_3, and their corresponding prime counterparts S_1', S_2', S_3'. Notably, the interatomic distance between S_3 and S_3' is measured at 4.65 Å, which exceeds that between S_2 and S_2' (4.56 Å) as shown in Figure 2a. Furthermore, the angle subtended by S_2, Au_2, and S_2' deviates significantly from the ideal linear geometry, registering at 173.53° as opposed to the expected 180° (see Figure 2b). This deviation can be ascribed to additional coordination of Au_2 with Au_3 and Au_3'.

The contraction in bond length and deviation from linearity can further be the consequence of surface interactions involving the phenyl rings as depicted in Figure 2c. Evident edge-to-face π–π stacking is discerned between phenyl rings PR_2 and SR_2', with 3.91 Å. A symmetrical interaction of similar nature is present between PR_2' and SR_2. In contrast, the phenyl rings PR_1 and PR_1' do not exhibit any intracluster interaction, which can be attributed to their extended separation, of 5.31 Å.

Generally, ultrasmall metal nanoclusters have distinct optical absorption UV-Vis spectra. In case of Au_4Cu_2 NC, the characteristics absorption peaks at 324 nm and 394 nm were maintained not only after stirring at room temperature (4 days) but also at higher temperature for 48 h as depicted in Figure S2, S3,

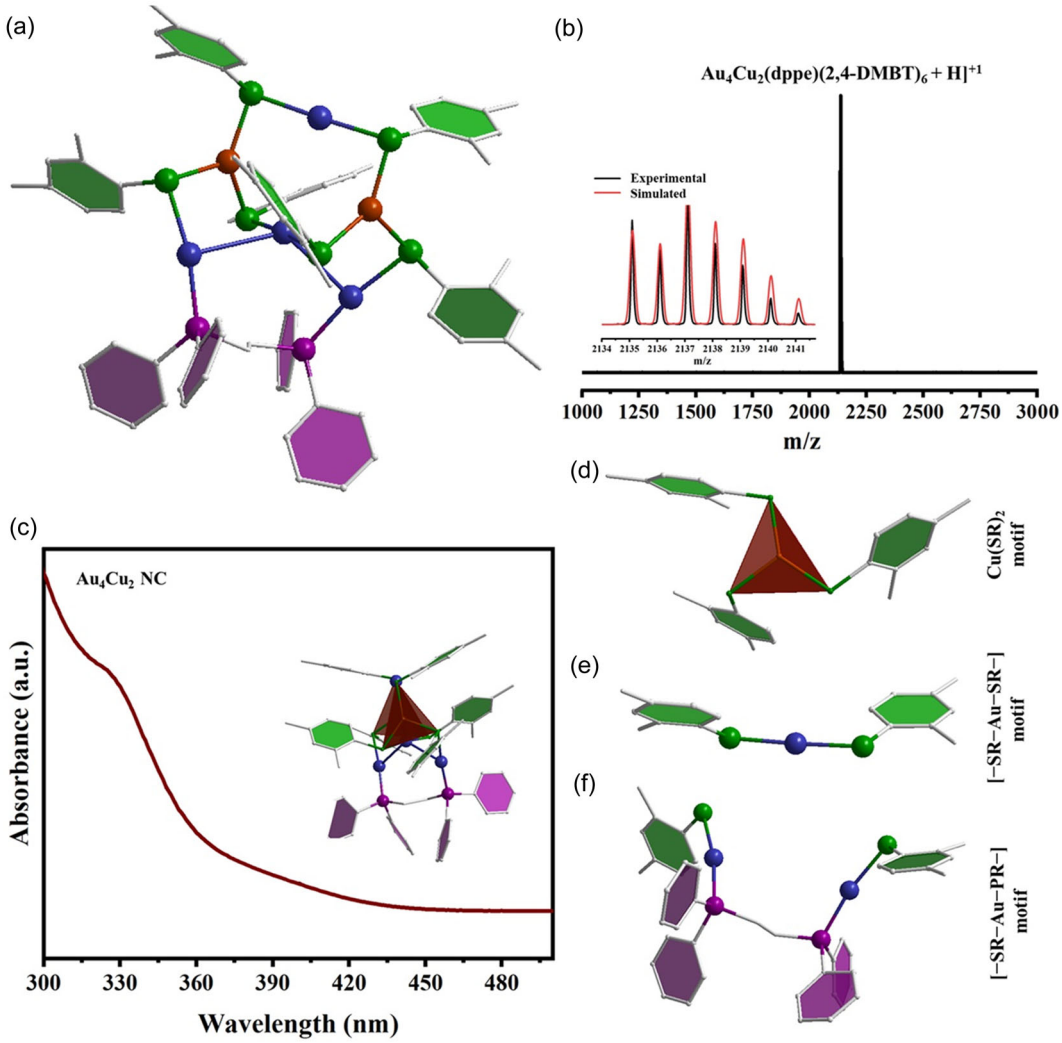

Figure 1. a) Structure of Au_4Cu_2 NC (color labels: blue, Au; maroon, Cu; green, S; magenta, p; gray, C), b) ESI-MS spectra of Au_4Cu_2 NC, c) UV-Vis absorption spectrum of Au_4Cu_2 NC, d) coordination mode of Cu with 2,4-DMBT, and e,f) coordination mode of Au with 2,4-DMBT and dppe, respectively.

Supporting Information, respectively, depicting the extraordinary stability of the cluster.

Au_4Cu_2 NC/Mo_2TiC_2 was engineered to examine the impact of integrating Au_4Cu_2 NC within the interlayer spacing of Mo_2TiC_2 MXene. A thorough analysis was conducted to compare the electrochemical behavior of the pristine Mo_2TiC_2 MXene and Au_4Cu_2 NC/Mo_2TiC_2 composite. Monolayered 2D Mo_2TiC_2 nanosheets were obtained via a modified chemical exfoliation method.[40–43] Au_4Cu_2 NC were then incorporated onto Mo_2TiC_2 MXene through chemical bath deposition technique under ambient conditions as shown in **Figure 3**a. A thin film of as-prepared Au_4Cu_2 NC/Mo_2TiC_2 composite was attained by vacuum-assisted filtration.

The dispersion and integration of Au_4Cu_2 NC within Mo_2TiC_2 MXene layers, forming a Au_4Cu_2 NC/Mo_2TiC_2 composite, were systematically analyzed via HRTEM, HAADF-STEM, and EDS (Figure 3b–h). HRTEM (Figure 3b) confirms successful exfoliation of monolayer Mo_2TiC_2 with interlayer stacking, validated by HAADF-STEM (Figure 3c). Pristine Mo_2TiC_2 exhibits a layered structure with 0.65 nm interlayer spacing as shown in Figure S4, Supporting Information.

Au_4Cu_2 NC appear as dark spots (red circles, Figure 3d), uniformly dispersed across MXene layers. In the cross-sectional view (Figure 3e), the metal nanocluster on the single-layered MXene acts as a bridge, preventing the MXene layers from restacking. The insertion of Au_4Cu_2 nanoclusters creates an interlayer spacing of 1.43 nm, as shown in Figure 3f,g, confirming the formation of the composite. The interface construction (Figure 3g) validates the anchoring of Au_4Cu_2 NC within the stacked MXene layers, serving as nanoscopic bridges. These nanoscopic bridges can facilitate the transport of electrons by providing conductive connectivity across stacked layers of MXene hence enhancing the charge storage ability capability of the MXene. Additionally, EDX analysis further confirmed the homogeneous dispersion of constituting elements Au, Cu, Mo, Ti, and C (Figure 3h), which validates the successful

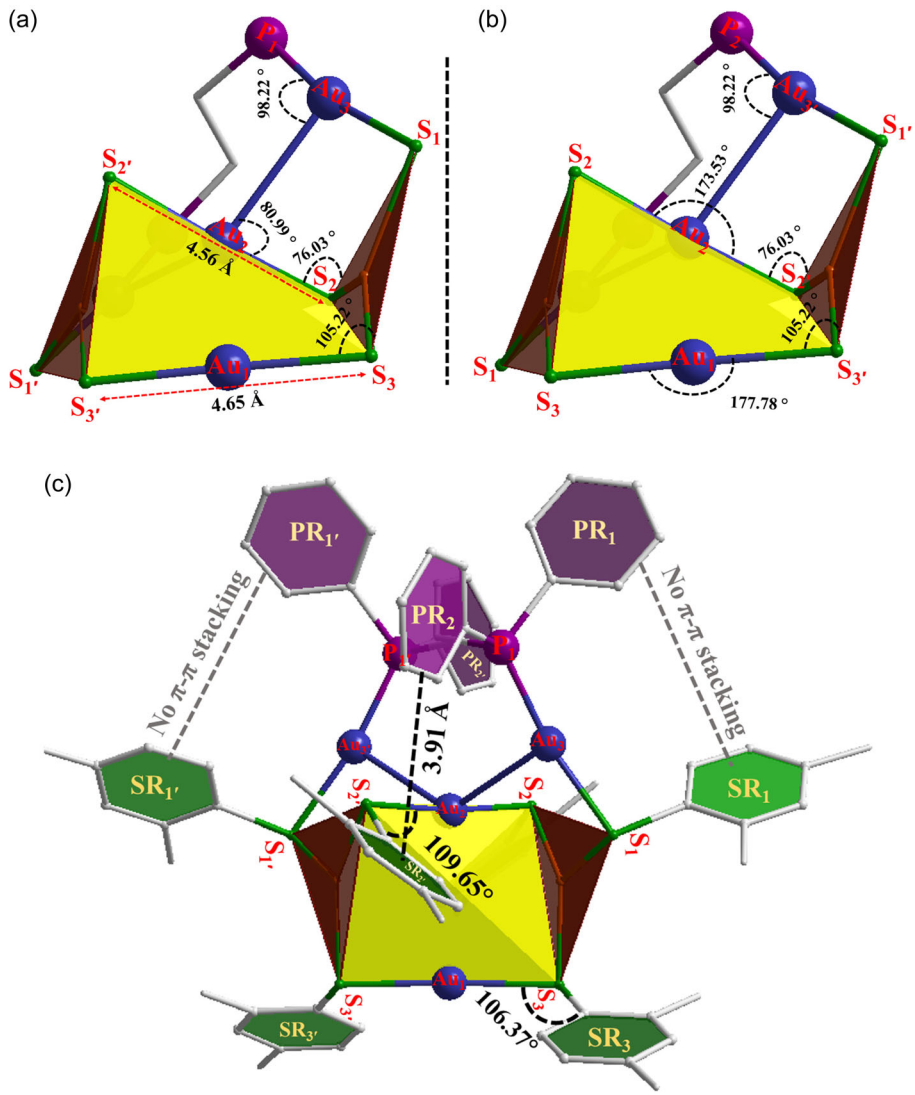

Figure 2. a,b) Anatomy of Au_4Cu_2 NC and c) detailed view of the edge to face π-π stacking in the $Cu(SR)_2$ motif with dppe. Color labels: blue, Au; maroon, Cu; green, S; magenta, p; and gray, C.

fabrication of the Au_4Cu_2 NC/Mo_2TiC_2. Furthermore, atomic force microscopy (AFM) was performed to investigate the roughness of Au_4Cu_2 NC/Mo_2TiC_2 as shown in Figure S5, Supporting Information. Surface roughness of Au_4Cu_2 NC/Mo_2TiC_2 was found at 101.3 nm which indicated a highly textured morphology.

To investigate whether the structural integrity of MXenes was preserved during integration, Powder X-ray diffraction (PXRD) was used. Figure S6, Supporting Information, depicts the PXRD patterns of the exfoliated pristine Mo_2TiC_2 MXene and Au_4Cu_2 NC/Mo_2TiC_2 composite. The exfoliated pristine Mo_2TiC_2 MXene exhibited diffraction peaks at 6.32°, 13. 97°, 16.80°, and 26.4° indexed to (2), (4), (6), and (10) planes, respectively. However, the diffraction peaks of Au_4Cu_2 NC/Mo_2TiC_2 composite depict higher intensity which suggests that the d-spacing values increased which can be ascribed to the integration of Au_4Cu_2 NC.[44] Moreover, no additional diffraction peaks from impurities appeared in the XRD patterns of Au_4Cu_2 NC/Mo_2TiC_2 composite. The unaltered PXRD patterns between Mo_2TiC_2 MXene and Au_4Cu_2 NC/Mo_2TiC_2 composite revealed that the structural morphology of the Mo_2TiC_2 MXene was retained with increased d spacing.

To determine the interaction between Au_4Cu_2 NC and Mo_2TiC_2 MXene, X-ray photoelectron spectroscopy (XPS) analysis of the Au 4*f*, Cu 2*p*, Ti 2*p*, and Mo 3*d* was conducted as presented in **Figure 4**. The characteristic peak of Au 4f at a binding energy of 84.38 eV (Au $4f_{7/2}$) and 88.08 eV (Au $4f_{5/2}$) in Au_4Cu_2 NC shifts to lower energies, 84.32 and 88.02 eV respectively, after integration with the Mo_2TiC_2, as shown in Figure 4a. Similar deviation was observed in case of Cu 2*p* where binding energy at 932.38 eV (Cu $2p_{3/2}$) and 952.28 eV (Cu $2p_{3/2}$) negatively shifted toward 932.27 eV (Cu $2p_{3/2}$) and 952.07 eV (Cu $2p_{3/2}$) after integration of Au_4Cu_2 NC across Mo_2TiC_2 MXene interlayers as shown in Figure 4b.[45] The significant negative shift

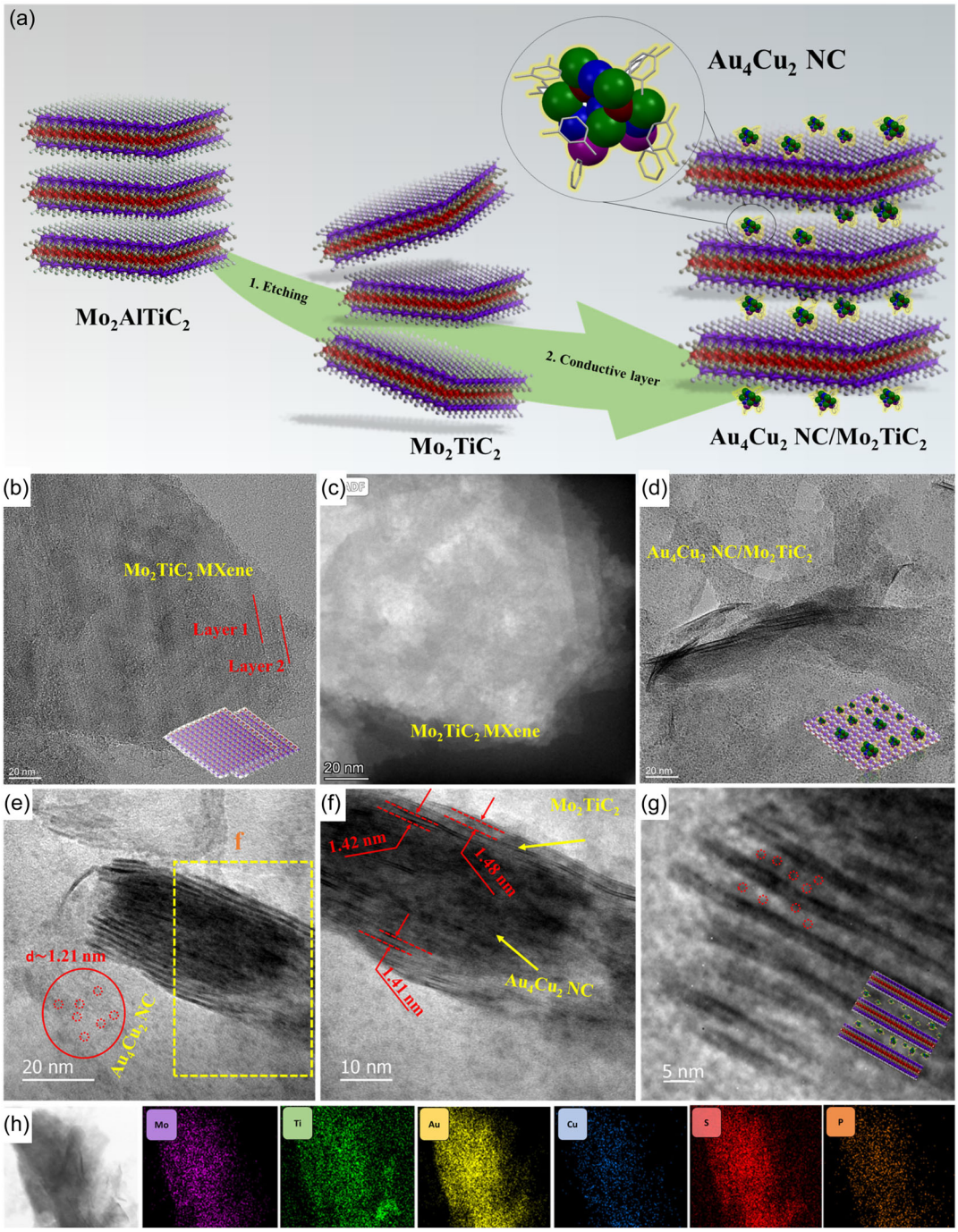

Figure 3. a) Schematic illustration for the integration of Au_4Cu_2 NC in Mo_2TiC_2 MXene, b) HRTEM image of Mo_2TiC_2 MXene, c) HAADF image of Mo_2TiC_2 MXene, and d) HRTEM image Au_4Cu_2 NC/Mo_2TiC_2 composite; surface view, e–g) cross-sectional view of Au_4Cu_2 NC/Mo_2TiC_2 composite, and h) EDX elemental mapping of Au_4Cu_2 NC/Mo_2TiC_2 composite showing constituting elements.

in binding energy of Au 4*f*, Cu 2*p* in Au_4Cu_2 NC/Mo_2TiC_2 composite, typically means the increase of surface electron density and most likely development of Van der Waals interactions Au_4Cu_2 NC and Mo_2TiC_2 MXene.[46] In terms of Mo_2TiC_2 MXene, the Ti 2*p* XPS spectrum can be divided into Ti—C bonds (454.98, 460.98 eV) and Ti—O bonds (458.08, 463.88 eV) as displayed in Figure 4c. The corresponding peaks of Ti 2*p* shift toward increasing binding energy in Au_4Cu_2 NC/Mo_2TiC_2 composite, that is, Ti—C bonds (455.48, 461.38 eV) and Ti—O bonds (458.68, 463.98 eV). Similar trend is observed in Mo 3*d* where the binding energy at 228.78 (Mo $3d_{5/2}$), 230.98 (Mo $3d_{3/2}$), 231.98 ($Mo^{5+/6+}$), and 235.18 eV ($Mo^{5+/6+}$) shifts positively after integration of Au_4Cu_2 NC across Mo_2TiC_2 MXene, as shown in Figure 4d.[42] The increase in binding energy of Mo 3*d* and Ti

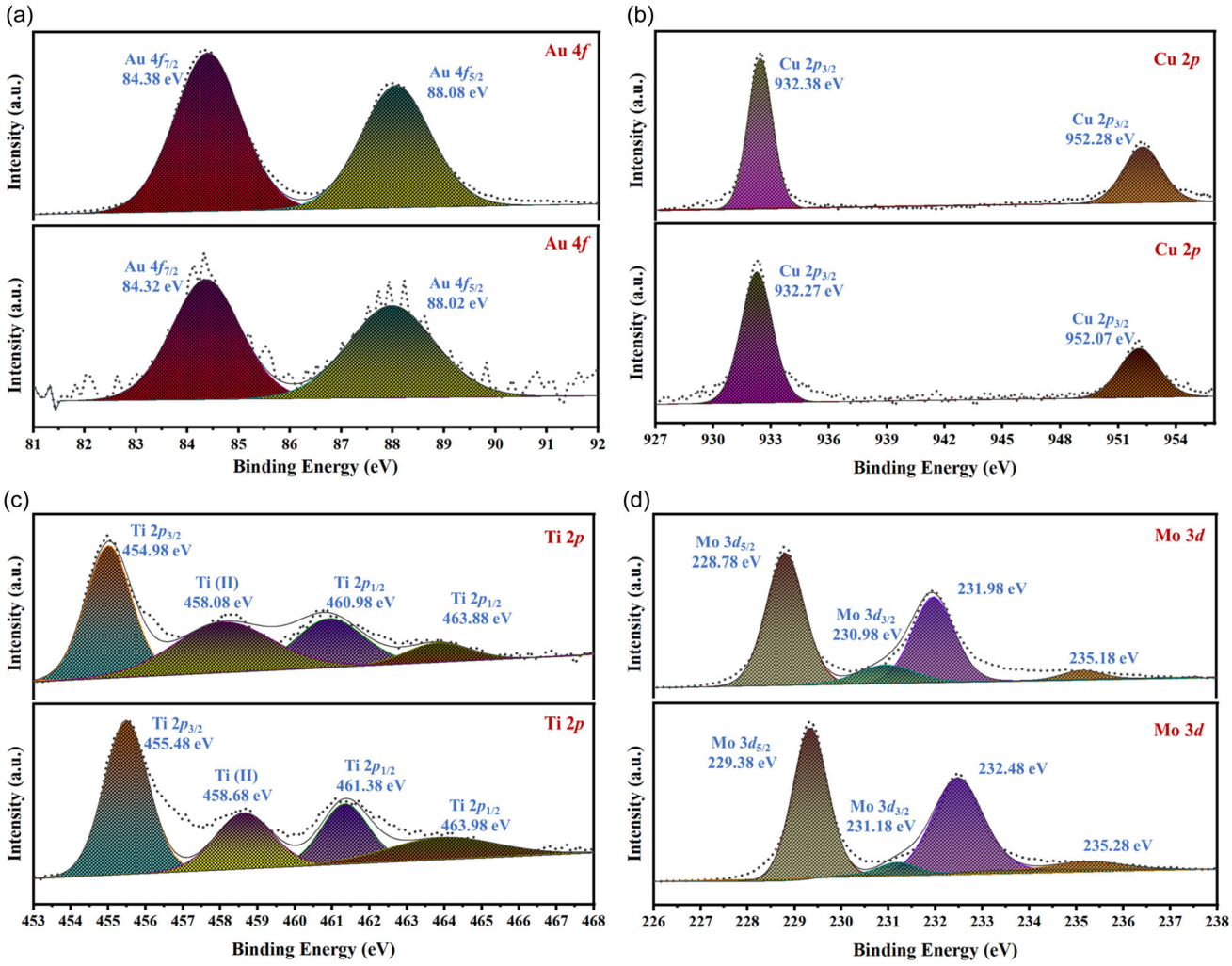

Figure 4. XPS spectra of a,b) Au_4Cu_2 NC (top) and Au_4Cu_2 NC/Mo_2TiC_2 composite (bottom) and c,d) Mo_2TiC_2 MXene (top) and Au_4Cu_2 NC/Mo_2TiC_2 composite (bottom).

2*p* in Au_4Cu_2 NC/Mo_2TiC_2 composite in comparison to Mo_2TiC_2 MXene signifies the development of Van der Waals interactions between Au_4Cu_2 NC Mo_2TiC_2 MXene. XPS analysis suggests that the electron transfers between Mo_2TiC_2 and Au_4Cu_2 NC develop a strong interaction and local coordination environment at the interlayer interface of MXene which is favorable for the transport of electron with reduced resistivity across the layers of MXene.

The electrochemical properties of Au_4Cu_2 NC/Mo_2TiC_2 composite and Mo_2TiC_2 MXene-based electrodes were predominantly explored by employing a three-electrode system via aqueous 3M KOH electrolyte and Hg/HgO as reference electrode. The inset of **Figure 5**a shows the CV of Au_4Cu_2 NC/Mo_2TiC_2 composite and Mo_2TiC_2 MXene at a scan rate of 30 mV s^{-1} across potential window ranging from −1 to 0.4 V. Evidently, the CV curve of Au_4Cu_2 NC/Mo_2TiC_2 composite exhibits a larger integrated area than Mo_2TiC_2 MXene. The better the integrated area, the more specific capacitance is compared to the Mo_2TiC_2 based electrode material. Moreover, as shown in Figure 5a, by comparing the discharging curve, it is evident that the potential window range of Au_4Cu_2 NC/Mo_2TiC_2 composite has increased significantly. The comparison of GCD profiles for Au_4Cu_2 NC/Mo_2TiC_2 composite to Mo_2TiC_2 MXene at a current density of 2 A g^{-1} shows a maintained potential window (Figure S7, Supporting Information). The Au_4Cu_2 NC/Mo_2TiC_2 composite displayed enhanced charge area and discharge time, illustrating a superior specific capacitance compared to Mo_2TiC_2 MXene. The CV curves of Au_4Cu_2 NC/Mo_2TiC_2 composite at 10 and 20 mV s^{-1} presented trapezoidal CV curve with redox peaks (Figure 5b), proving that the composites exhibited Faradaic pseudocapacitive behaviors. Moreover, with an increase in scan rate from 10 to 20 mV s^{-1}, an increased integrated area of the CV curves in both the cathodic and anodic regions is observed. Specific capacity of Au_4Cu_2 NC/Mo_2TiC_2 composite and Mo_2TiC_2 MXene were determined by using Equation (1)[47–49] and compared altered current density ranging from (2 to 10 A g^{-1}) as displayed in Figure 5c.

$$C = \frac{I\Delta t}{m} \tag{1}$$

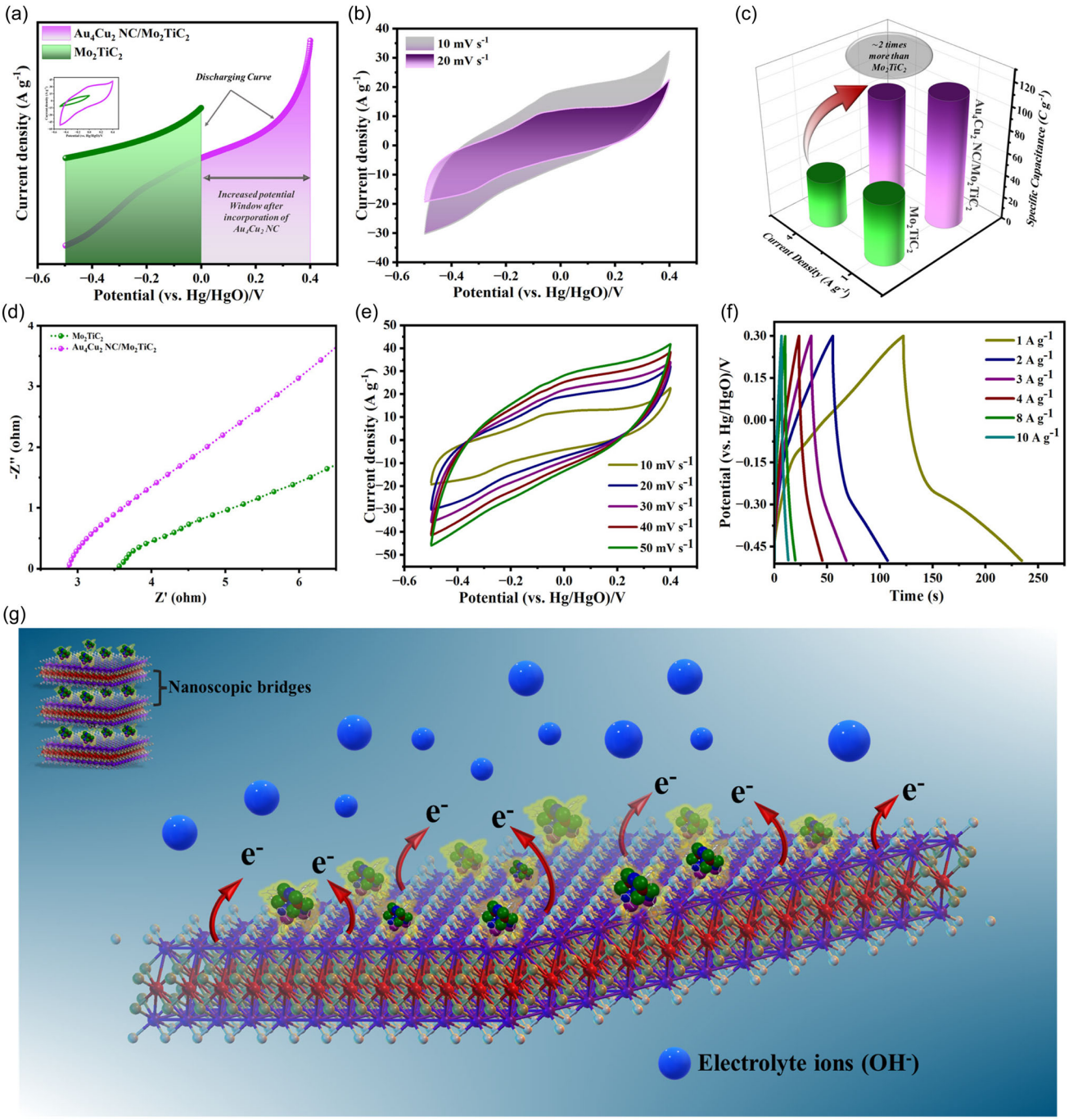

Figure 5. Comparison of Mo_2TiC_2 MXene and Au_4Cu_2 NC/Mo_2TiC_2 composite, a) cyclic voltammetry curves at 30 mV s^{-1}, b) comparative analysis of Au_4Cu_2 NC/Mo_2TiC_2 composite CV curves at 10 and 20 mV s^{-1}, c) specific capacitance at different current densities ranging from 2 to 4 A g^{-1} current density, and d) ESR plot of Mo_2TiC_2 MXene and Au_4Cu_2 NC/Mo_2TiC_2 composite. e) CV curves Au_4Cu_2 NC/Mo_2TiC_2 composite, f) GCD curves of Au_4Cu_2 NC/Mo_2TiC_2 composite, and g) schematic depiction of the charge storage mechanism of Au_4Cu_2 NC/Mo_2TiC_2 composite.

where C (C g^{-1}) = specific capacity of electrode material; I (A) = current provided while discharge process; Δt (s) = discharge time of electrode material; and m (g) = the mass of the active materials (i.e., Au_4Cu_2 NC/Mo_2TiC_2 composite and Mo_2TiC_2 MXene).

Mo_2TiC_2 MXene showed lower specific capacitance which was increased 2.07 times after the addition of atomically precise ultrasmall Au_4Cu_2 NC. Even at enhanced current density of 4 A g^{-1}, Au_4Cu_2 NC/Mo_2TiC_2 composite leads the specific capacitance of 88.0 C g^{-1}; meanwhile, Mo_2TiC_2 MXene depicted specific capacitance of 41.0 C g^{-1}, respectively, demonstrated in Figure 5c. The enhanced specific capacitance observed can be attributed to the incorporation of Au_4Cu_2 NC within Mo_2TiC_2.

Detailed CVs of Au_4Cu_2 NC/Mo_2TiC_2 composite were attained at various scan rates (5–50 mV s^{-1}) presented in Figure 5e. It is apparent that the current density area of voltammogram enhanced by enhancing the scan rate from 5 to 50 mV s^{-1} denoting the polarization of NC, improved ions, and electrons mobility rates, and a similar pattern has been exhibited with the other electrode as displayed in Figure S8, Supporting Information. CV with a symmetric nature even at an enhanced scan rate denotes rapid redox reaction levels, enhanced reversibility, and efficient rate capability.[50–52] Figure 5f displays the thorough GCD profiles of Au_4Cu_2 NC/Mo_2TiC_2 composite, and Figure S9, Supporting Information, corresponds to the detailed GCD curves of Mo_2TiC_2 MXene, respectively. From GCD profiles, significant voltage drop can be easily observed which likely stems from increased internal resistance which can be attributed to the interactions between the composite and binder, which could hinder charge transfer efficiency.[53,54] The Au_4Cu_2 NC/Mo_2TiC_2 composite exhibited a 79% stability retention at 8000 cycles (2 A g^{-1}) with 99% which demonstrates excellent electrode material for energy storage applications (Figure S10, Supporting Information).

Electrochemical impedance spectroscopy (EIS) data of both electrodes (i.e., Au_4Cu_2 NC/Mo_2TiC_2 composite, and Mo_2TiC_2 MXene) were analyzed and displayed in Figure 5d. Equivalent series resistance (ESR) is stated as the intercept in the real axis at the increased frequency area, designated as solution resistance that links the resistance of electrode active material, electrolyte, and contact among active material/current collector.[55,56] Here, a straight line in a low frequency area signifies Warburg resistance, that is, resistance between electrode/electrolyte boundary or interface and the movement of electrolyte at surface/pores of electrode materials (characteristics of the capacitance behavior), respectively.[57] Compared to the Mo_2TiC_2 MXene, the integrated Au_4Cu_2 NC/Mo_2TiC_2 composite demonstrated a low ESR value, which supports its diminished resistivity and improved conductivity. Established on EIS analysis, the Au_4Cu_2 NC may have reduced the resistance and increased the conductivity of MXene, which provides enhanced capacitance.

The enhanced electrochemical performance of Au_4Cu_2 NC/Mo_2TiC_2 composite can be ascribed to the following factors: First, the introduction of Au_4Cu_2 NC in the interlayer spacing of Mo_2TiC_2 MXene prevents restacking of MXene. Second, Au_4Cu_2 NC provide additional conductive pathways keeping the integrity of the characteristic lamellar structure of MXene. Au_4Cu_2 NC with nano sizes allows them to fit within the MXene layers, effectively bridging gaps and improving overall conductivity by acting as nanoscopic bridges. This synergy between MXenes and nanoclusters results in superior capacitance of Au_4Cu_2 NC/Mo_2TiC_2 composite, by providing conductive channels resulting in reduced resistivity of the electrode material. The results demonstrate that the incorporation of nanoscopic bridges to prevent the development of interlayer

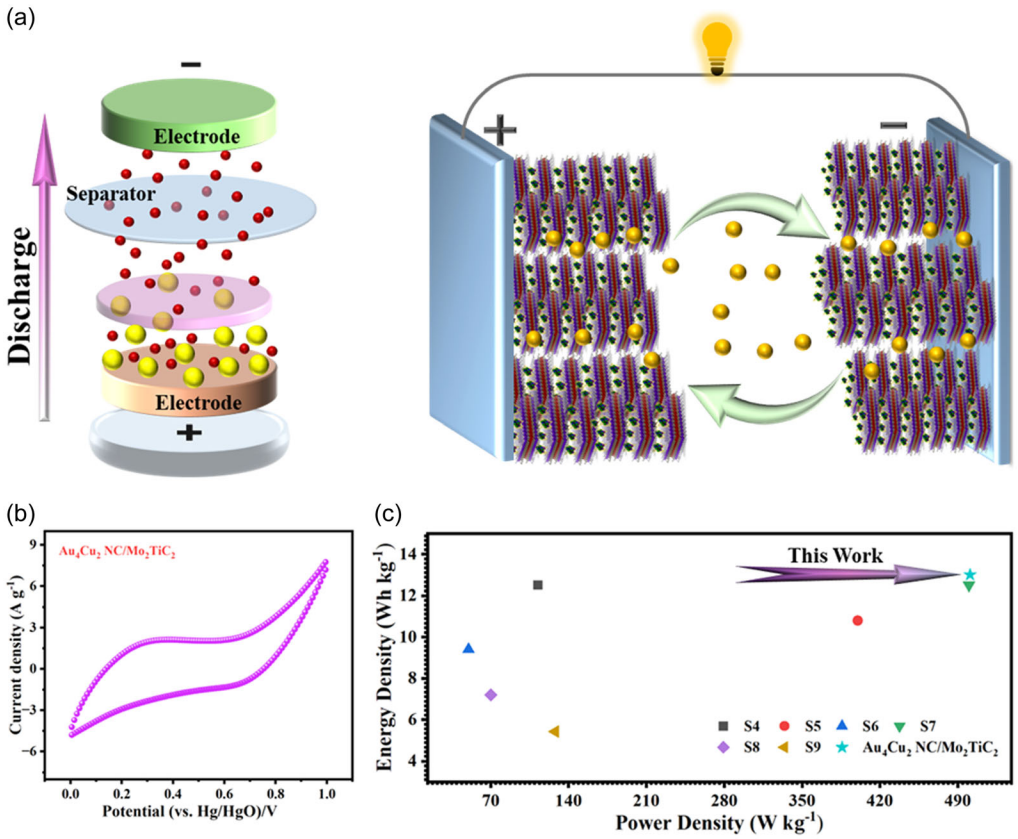

Figure 6. a) Schematic illustration of the Au_4Cu_2 NC/Mo_2TiC_2 based symmetric device configuration (positive and negative electrode). b) Preliminary CV curve in three-electrode measurements system at 10 mV s^{-1}. c) Ragone plot of the SSC device Au_4Cu_2 NC/Mo_2TiC_2.

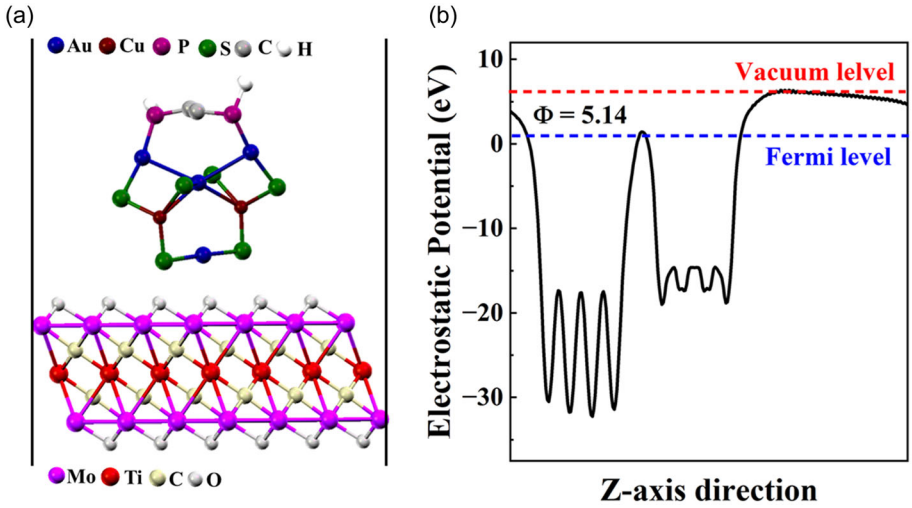

Figure 7. a) Optimized Au_4Cu_2 NC/Mo_2TiC_2 composite and b) the associated electrostatic potential. Here, the vacuum level and Fermi level are represented by blue and red dashed lines, respectively.

conductive junctions in 2D materials can be an efficient strategy to enhance the electrochemical performance of 2D materials. Schematic representation for charge storage mechanism of Au_4Cu_2 NC/Mo_2TiC_2 composite is demonstrated in Figure 5g.

The findings support the practical application of Au_4Cu_2 NC/Mo_2TiC_2 as efficient electrodes in a symmetric supercapacitor (SSC) (see **Figure 6**a). The SSC device demonstrated an increased operating voltage of 1 V (Figure 6b), with the reproducibility of the CV at various scan rates illustrated in Figure S11, Supporting Information. The symmetric CV profiles at varying current densities indicate minimal polarization, ascribed to the Au_4Cu_2 NC/Mo_2TiC_2 composite enhanced conductivity and ion diffusion. The detailed GCD profile of Au_4Cu_2 NC/Mo_2TiC_2 based SSC is shown in Figure S12, Supporting Information. The Nyquist plot for the Au_4Cu_2 NC/Mo_2TiC_2 composite based SSC device demonstrates a semicircle at high frequencies and a Warburg tail at low frequencies as shown in Figure S13, Supporting Information. From circuit model fitting, R(Q(RW)) fits the data; see inset of Figure S13, Supporting Information. Moreover, Au_4Cu_2 NC/Mo_2TiC_2 composite based SSC demonstrates exceptional stability for 500 cycles at 4 A g^{-1} with Coulumbic efficiency of 96%, indicating minimal energy loss during charge/discharge as shown in Figure S14, Supporting Information. This result can be attributed to the expanded interlayer spacing which facilitates rapid ion, and the conductive Au_4Cu_2 NC that bridges layers of MXene, reducing interlayer resistance. Furthermore, The Ragone plot, shown in Figure 6c, indicates appreciable energy and power densities compared to previously reported devices (refer to Table S1, Supporting Information). The energy density attained as 13 W kg^{-1} at power density of 501 Wh kg^{-1}. This indicates that Au_4Cu_2 NC/Mo_2TiC_2 can be utilized directly and completely integrated as an SSC device requiring no additional modifications, thus minimizing preparation time and material costs while maintaining performance. This highlights the practical applicability of the prepared Au_4Cu_2 NC/Mo_2TiC_2-based composite.

To further elucidate the charge transfer mechanism within the Au_4Cu_2 NC/Mo_2TiC_2 composite, we analyzed the electrostatic potential using DFT calculations. The work function (Φ) represents the minimum energy required to remove an electron from a material's surface to the vacuum level, directly influencing charge transfer efficiency at the heterojunction. From Figure S15, Supporting Information, Mo_2TiC_2 exhibits a relatively high work function of 6.32 eV, while the work function of Au_4Cu_2 NC is around 3.80 eV. The formation of a heterostructure at the interface between Mo_2TiC_2 and Au_4Cu_2 NC results in an intermediate work function of 5.14 eV (see **Figure 7**), which governs electron movement and charge redistribution across the interface. This energy offset enables electron transfer between Au_4Cu_2 NC and Mo_2TiC_2. The electrostatic potential difference further validates the superior charge transport properties observed in Au_4Cu_2 NC/Mo_2TiC_2 composite-based electrodes, enhancing the material's potential for high-performance supercapacitor applications.

3. Conclusion

To conclude, we successfully synthesized ultrasmall bimetallic Au_4Cu_2 NC through a two-phase synthesis method. The structure characterization of these nanoclusters was confirmed by SCXRD and ESI-MS. The Au_4Cu_2 NC were then incorporated into the Mo_2TiC_2 MXene using local coordination techniques, where Au_4Cu_2 NC functioned as nanoscopic bridges. These bridges play a dual role: they mitigate the restacking of MXene layers and improve conductivity within the structure. The incorporation of Au_4Cu_2 NC into the Mo_2TiC_2 MXene matrix resulted in a significant enhancement of specific capacitance when compared to the standalone Mo_2TiC_2 MXene. This improvement underscores the efficacy of our interfacial engineering approach, which leverages the synergistic properties of MXenes and metal nanoclusters. Au_4Cu_2 NC/Mo_2TiC_2 composite based SSC provided a high energy density of 13 W kg^{-1}

at a power density of 501 Wh kg^{-1}. Ultimately, our study advances the field of energy storage by presenting a sophisticated strategy for engineering the interfaces of layered materials, significantly boosting their charge storage capacities, and pushing the boundaries of performance for next-generation energy storage systems.

Accession Codes

CCDC 2157098 contains the supplementary crystallographic data for this paper. This data can be obtained free of charge via www.ccdc.cam.ac.UK/data_request/cif, or by emailing data_request@ccdc.cam.ac.UK, or by contacting The Cambridge Crystallographic Data Centre, 12 Union Road, Cambridge CB2 1EZ, UK; fax: +44 1223 336033.

Supporting Information

Supporting Information is available from the Wiley Online Library or from the author.

Acknowledgements

The authors gratefully acknowledge The University of Hong Kong, the Research Grants Council of the Hong Kong Special Administrative Region, People's Republic of China (RGC: 27301820 and 17313922), the Croucher Foundation, the Innovation and Technology Commission (HKSAR, China), the National Natural Science Foundation of China (No. 22201236), and Donations for Research Projects_RMGS (project number 9229006) for their financial support.

Conflict of Interest

The authors declare no conflict of interest.

Author Contributions

Tehseen Nawaz: writing—original draft (lead); methdology (lead); writing—review and editing (lead). **Muhammad Ahmad**: supervision (lead); writing—review and editing (lead). **Iftikhar Hussain**: methodology (supporting); supervision (supporting). **Xi Chen**: investigation (supporting); methodology (supporting); software (supporting). **B. Moses Abraham**: software (lead). **Shengli Zhuang**: software (supporting). **Kam Hung Low**: software (equal). **Kaili Zhang**: supervision (lead). **Jian He**: supervision (equal).

Data Availability Statement

The data that support the findings of this study are available from the corresponding author upon reasonable request.

Keywords

metal nanoclusters, Mo_2TiC_2, MXene, nanoscopic bridges, supercapacitors

Received: December 18, 2024
Revised: February 17, 2025
Published online:

[1] N. Mounet, M. Gibertini, P. Schwaller, D. Campi, A. Merkys, A. Marrazzo, T. Sohier, I. E. Castelli, A. Cepellotti, G. Pizzi, N. Marzari, *Nat. Nanotechnol.* **2018**, *13*, 246.
[2] S. Das, H.-Y. Chen, A. V. Penumatcha, J. Appenzeller, *Nano Lett.* **2013**, *13*, 100.
[3] Y. Zhang, J. Ye, Y. Matsuhashi, Y. Iwasa, *Nano Lett.* **2012**, *12*, 1136.
[4] A. G. Kelly, T. Hallam, C. Backes, A. Harvey, A. S. Esmaeily, I. Godwin, J. Coelho, V. Nicolosi, J. Lauth, A. Kulkarni, S. Kinge, L. D. A. Siebbeles, G. S. Duesberg, J. N. Coleman, *Science* **2017**, *356*, 69.
[5] T. M. Higgins, S. Finn, M. Matthiesen, S. Grieger, K. Synnatschke, M. Brohmann, M. Rother, C. Backes, J. Zaumseil, *Adv. Funct. Mater.* **2019**, *29*, 1804387.
[6] D. J. Finn, M. Lotya, G. Cunningham, R. J. Smith, D. Mccloskey, J. F. Donegan, J. N. Coleman, *J. Mater. Chem. C* **2014**, *2*, 925.
[7] S. Ghosh, A. Winchester, B. Muchharla, M. Wasala, S. Feng, A. L. Elias, M. B. M. Krishna, T. Harada, C. Chin, K. Dani, S. Kar, M. Terrones, S. Talapatra, *Sci. Rep.* **2015**, *5*, 11272.
[8] R. Worsley, L. Pimpolari, D. Mcmanus, N. Ge, R. Ionescu, J. A. Wittkopf, A. Alieva, G. Basso, M. Macucci, G. Iannaccone, K. S. Novoselov, H. Holder, G. Fiori, C. Casiraghi, *ACS Nano* **2019**, *13*, 54.
[9] T. Carey, S. Cacovich, G. Divitini, J. Ren, A. Mansouri, J. M. Kim, C. Wang, C. Ducati, R. Sordan, F. Torrisi, *Nat. Commun.* **2017**, *8*, 1202.
[10] C. Zhang, L. Mckeon, M. P. Kremer, S.-H. Park, O. Ronan, A. Seral-Ascaso, S. Barwich, C. Ó. Coileáin, N. Mcevoy, H. C. Nerl, B. Anasori, J. N. Coleman, Y. Gogotsi, V. Nicolosi, *Nat. Commun.* **2019**, *10*, 1795.
[11] K. Parvez, Z.-S. Wu, R. Li, X. Liu, R. Graf, X. Feng, K. Müllen, *J. Am. Chem. Soc.* **2014**, *136*, 6083.
[12] A. Vahidmohammadi, J. Rosen, Y. Gogotsi, *Science* **2021**, *372*, eabf1581.
[13] B. Anasori, Y. Gogotsi, *Graphene 2D Mater.* **2022**, *7*, 75.
[14] X. Li, Z. Huang, C. E. Shuck, G. Liang, Y. Gogotsi, C. Zhi, *Nat. Rev. Chem.* **2022**, *6*, 389.
[15] J. Nan, X. Guo, J. Xiao, X. Li, W. Chen, W. Wu, H. Liu, Y. Wang, M. Wu, G. Wang, *Small* **2021**, *17*, 1902085.
[16] K. Li, M. Liang, H. Wang, X. Wang, Y. Huang, J. Coelho, S. Pinilla, Y. Zhang, F. Qi, V. Nicolosi, Y. Xu, *Adv. Funct. Mater.* **2020**, *30*, 2000842.
[17] J. Tang, T. S. Mathis, N. Kurra, A. Sarycheva, X. Xiao, M. N. Hedhili, Q. Jiang, H. N. Alshareef, B. Xu, F. Pan, Y. Gogotsi, *Angew. Chem.* **2019**, *131*, 18013.
[18] M. Saraf, T. Zhang, T. Averianov, C. E. Shuck, R. W. Lord, E. Pomerantseva, Y. Gogotsi, *Small Methods* **2023**, *7*, 2201551.
[19] W. Lv, G. Wu, X. Li, J. Li, Z. Li, *Energy Storage Mater.* **2022**, *46*, 138.
[20] C. Wang, S. Chen, H. Xie, S. Wei, C. Wu, L. Song, *Adv. Energy Mater.* **2019**, *9*, 1802977.
[21] M. Wang, Y. Cheng, H. Zhang, F. Cheng, Y. Wang, T. Huang, Z. Wei, Y. Zhang, B. Ge, Y. Ma, Y. Yue, Y. Gao, *Adv. Funct. Mater.* **2023**, *33*, 2211199.
[22] B. Anasori, Y. Xie, M. Beidaghi, J. Lu, B. C. Hosler, L. Hultman, P. R. C. Kent, Y. Gogotsi, M. W. Barsoum, *ACS Nano* **2015**, *9*, 9507.
[23] Y. Fang, R. Hu, K. Zhu, K. Ye, J. Yan, G. Wang, D. Cao, *Adv. Funct. Mater.* **2020**, *30*, 2005663.
[24] X. Zang, J. Wang, Y. Qin, T. Wang, C. He, Q. Shao, H. Zhu, N. Cao, *Nano-Micro Lett.* **2020**, *12*, 1.
[25] Z. Wu, X. Liu, T. Shang, Y. Deng, N. Wang, X. Dong, J. Zhao, D. Chen, Y. Tao, Q. Yang, *Adv. Funct. Mater.* **2021**, *31*, 2102874.
[26] H. Shi, M. Yue, C. J. Zhang, Y. Dong, P. Lu, S. Zheng, H. Huang, J. Chen, P. Wen, Z. Xu, Q. Zheng, X. Li, Y. Yu, Z.-S. Wu, *ACS Nano* **2020**, *14*, 8678.
[27] T. Shang, Z. Lin, C. Qi, X. Liu, P. Li, Y. Tao, Z. Wu, D. Li, P. Simon, Q. Yang, *Adv. Funct. Mater.* **2019**, *29*, 1903960.

[28] Y. Deng, T. Shang, Z. Wu, Y. Tao, C. Luo, J. Liang, D. Han, R. Lyu, C. Qi, W. Lv, F. Kang, Q. Yang, *Adv. Mater.* **2019**, *31*, 1902432.
[29] F. Bu, M. M. Zagho, Y. Ibrahim, B. Ma, A. Elzatahry, D. Zhao, *Nano Today* **2020**, *30*, 100803.
[30] K. Liang, R. A. Matsumoto, W. Zhao, N. C. Osti, I. Popov, B. P. Thapaliya, S. Fleischmann, S. Misra, K. Prenger, M. Tyagi, E. Mamontov, V. Augustyn, R. R. Unocic, A. P. Sokolov, S. Dai, P. T. Cummings, M. Naguib, *Adv. Funct. Mater.* **2021**, *31*, 2104007.
[31] L. Shen, X. Zhou, X. Zhang, Y. Zhang, Y. Liu, W. Wang, W. Si, X. Dong, *J. Mater. Chem. A* **2018**, *6*, 23513.
[32] W. Zheng, J. Halim, A. El Ghazaly, A. S. Etman, E. N. Tseng, P. O. Persson, J. Rosen, M. W. Barsoum, *Adv. Sci.* **2021**, *8*, 2003656.
[33] I. Chakraborty, T. Pradeep, *Chem. Rev.* **2017**, *117*, 8208.
[34] R. Jin, C. Zeng, M. Zhou, Y. Chen, *Chem. Rev.* **2016**, *116*, 10346.
[35] X. Kang, H. Chong, M. M. Zhu, *Nanoscale.* **2018**, *10*, 10758.
[36] Z. Lei, X.-K. Wan, S.-F. Yuan, Z.-J. Guan, Q.-M. Wang, *Acc. Chem. Res.* **2018**, *51*, 2465.
[37] R. Jin, *Nanoscale* **2015**, *7*, 1549.
[38] X. Kang, M. Zhu, *Chem. Soc. Rev.* **2019**, *48*, 2422.
[39] Y.-L. Li, Z.-Y. Wang, X.-H. Ma, P. Luo, C.-X. Du, S.-Q. Zang, *Nanoscale* **2019**, *11*, 5151.
[40] B. Anasori, M. R. Lukatskaya, Y. Gogotsi, *Nat. Rev. Mater.* **2017**, *2*, 1.
[41] W. Peng, M. Luo, X. Xu, K. Jiang, M. Peng, D. Chen, T. Chan, Y. Tan, *Adv. Energy Mater.* **2020**, *10*, 2001364.
[42] J. Zhang, Y. Zhao, X. Guo, C. Chen, C.-L. Dong, R.-S. Liu, C.-P. Han, Y. Li, Y. Gogotsi, G. Wang, *Nat. Catal.* **2018**, *1*, 985.
[43] J. Zhang, Z. Lin, Y. Lan, G. Ren, D. Chen, F. Huang, M. Hong, *J. Am. Chem. Soc.* **2006**, *128*, 12981.
[44] M. Saraf, B. Chacon, S. Ippolito, R. W. Lord, M. Anayee, R. Wang, A. Inman, C. E. Shuck, Y. Gogotsi, *Adv. Funct. Mater.* **2024**, *34*, 2306815.
[45] H. Yu, M. Dai, J. Zhang, W. Chen, Q. Jin, S. Wang, Z. He, *Small* **2023**, *19*, 2205767.
[46] K. Huang, C. Li, X. Meng, *J. Colloid Interface Sci.* **2020**, *580*, 669.
[47] L.-Q. Mai, A. Minhas-Khan, X. Tian, K. M. Hercule, Y.-L. Zhao, X. Lin, X. Xu, *Nat. Commun.* **2013**, *4*, 2923.
[48] P. Sivakumar, M. Jana, M. Kota, M. G. Jung, A. Gedanken, H. S. Park, *J. Power Sources.* **2018**, *402*, 147.
[49] I. Hussain, S. G. Mohamed, A. Ali, N. Abbas, S. M. Ammar, W. Al Zoubi, *J. Electroanal. Chem.* **2019**, *837*, 39.
[50] M. Ahmad, I. Hussain, T. Nawaz, Y. Li, X. Chen, S. Ali, M. Imran, X. Ma, K. Zhang, *J. Power Sources* **2022**, *534*, 231414.
[51] I. Hussain, T. Hussain, S. B. Ahmed, T. Kaewmaraya, M. Ahmad, X. Chen, M. S. Javed, C. Lamiel, K. Zhang, *J. Power Sources* **2021**, *513*, 230556.
[52] I. Hussain, S. Iqbal, T. Hussain, Y. Chen, M. Ahmad, M. S. Javed, A. Alfantazi, K. Zhang, *J. Mater. Chem. A* **2021**, *9*, 17790.
[53] W. G. Nunes, B. G. A. Freitas, R. M. Beraldo, R. M. Filho, L. M. Da Silva, H. Zanin, *Sci. Rep.* **2020**, *10*, 19195.
[54] C. Liu, Z G. Neale, G. Cao, *Mater. Today* **2016**, *19*, 109.
[55] I. Hussain, A. Ali, C. Lamiel, S. G. Mohamed, S. Sahoo, J.-J. Shim, *Dalton Trans.* **2019**, *48*, 3853.
[56] I. Hussain, S. Sahoo, D. Mohapatra, M. Ahmad, S. Iqbal, M. S. Javed, S. Gu, N. Qin, C. Lamiel, K. Zhang, *Appl. Mater. Today* **2022**, *26*, 101297.
[57] M. Manikandan, K. Subramani, S. Dhanuskodi, M. Sathish, *Energy Fuels* **2021**, *35*, 12527.